Nonlinear Dyn
https://doi.org/10.1007/s11071-025-11038-x

RESEARCH

Self-sustained and oscillatory activity in two types of attractor networks

Tao Wang · Jun-Xiang Gui · Mengjiao Zuo · Wei Wang · Feng Liu

Received: 29 November 2024 / Accepted: 21 February 2025

Abstract While self-sustained firing activity has been a primary focus in studies of attractor networks, the occurrence of neural rhythms within these networks has received comparatively less attention. Here, we employ mean-field models to investigate the emergence of intrinsic oscillations in two types of attractor networks, simplified from those underlying working memory and grid cell functionality. The networks consist of either two excitatory populations and one inhibitory population or two excitatory and two inhibitory populations, capable of self-sustained activity through self-excitation and self-disinhibition mechanisms, respectively. Both networks can exhibit eight distinct dynamic behaviors, with various bifurcation routes driving state transitions. Of particular biological relevance are oscillations coexisting with self-sustained activity. Self-sustained oscillations result from negative feedback between activated excitatory and inhibitory populations. Our analysis reveals how network connectivity, synaptic receptor types, background input, and noise modulate the self-sustainability, oscillations, and state stability. Notably, the self-disinhibition mechanism confers greater robustness and flexibility in maintaining both the self-sustained and oscillatory activity. This work highlights the intrinsic oscillatory nature of attractor networks, revealing universal principles that govern these processes and demonstrating the importance of network connectivity in shaping network dynamics and robustness. These findings contribute to a deeper understanding of neural rhythm in cognitive functions.

Keywords Attractor network · Self-sustained activity · Intrinsic oscillation · Bifurcation analysis · Working memory · Grid cell

1 Introduction

Attractor networks have long served as a prominent computational framework in neuroscience [1–3]. These networks arise from abundant synaptic connections among neurons, which constrain high-dimensional neuronal activity to low-dimensional attractive manifolds in state space, including points, rings, tori, and other complex geometries [4, 5]; neural states are drawn toward these manifolds regardless of their initial conditions. The robustness of attractor manifolds against noise and distractions enables efficient

T. Wang · J.-X. Gui · W. Wang (✉) · F. Liu (✉)
National Laboratory of Solid State Microstructures, Department of Physics, Collaborative Innovation Center of Advanced Microstructures, and Institute for Brain Sciences, Nanjing University, Nanjing 210093, China
e-mail: wangwei@nju.edu.cn

F. Liu
e-mail: fliu@nju.edu.cn

M. Zuo
Kuang Yaming Honors School, Nanjing University, Nanjing 210023, China

Published online: 17 March 2025

and stable information representation, which is critical for various brain functions including memory, decision-making, and spatial navigation [1–3]. A classic example of attractor dynamics is the self-sustained firing of a localized neuron population within a network; different populations correspond to distinct attractor states, encoding different pieces of information. This dynamic interplay is governed by the balance between excitation and inhibition, with global inhibition counteracting local excitation or disinhibition [1, 3, 5, 6]. Empirical evidence confirms the existence and functional significance of attractor networks in brain regions [1, 6–10]. For example, ring attractor networks in the prefrontal cortex support the locally self-sustained activity underlying visuospatial working memory (WM) [1]. Similarly, head-direction cells in the posterior subiculum and anterior dorsal nucleus rely on ring attractor networks to represent heading direction, while grid cells (GCs) in the medial entorhinal cortex use toroidal attractor networks to encode spatial location [11, 12].

Apart from self-sustained activity, accumulating evidence highlights the roles of neural oscillations in cognitive processes [13–15]. In working memory tasks, bursts of gamma oscillations emerge during the loading and processing of memory items [15]. During spatial navigation, spike phase-locking and phase precession relative to the theta rhythm in local field potential are observed in place cells and grid cells [16, 17], which is considered important for integrating spatial and temporal information [18, 19]. However, current attractor network models struggle to explain the origins and functions of these rhythms. Oscillations were typically introduced phenomenologically when needed [14, 20]. This limitation has motivated alternative theories incorporating oscillation-driven mechanisms for these neural functions. It was suggested that working memory is maintained by the coupling of theta and gamma oscillations [21, 22] and periodic firing fields of grid cells result from the interference of multiple theta waves [23, 24]. Despite their appeal, these oscillation-based theories often lack strong experimental support, in contrast to the extensive evidence for attractor networks [6, 8, 10, 11]. To advance our understanding of these cognitive functions, it is essential to integrate the self-sustained and rhythmic activity within a unified framework.

Neural oscillations are a ubiquitous feature of brain activity, and various mechanisms have been proposed for their generation, such as pacemaker neurons, local circuit interactions, and rhythmic inputs from other regions [25–32]. At their core, oscillations stem from three key ingredients: negative feedback, sufficient nonlinearity, and adequate time delay [33, 34]. Interestingly, attractor networks naturally embody these components. Recurrent connections between excitatory and inhibitory neurons constitute negative feedback loops [6, 14]. Nonlinear neuronal and synaptic responses facilitate dynamic interactions. Synaptic currents, especially those mediated by NMDA receptors, contribute to the necessary time delays [35, 36]. In attractor networks, oscillations often emerge as global phenomena, involving coherent activity of activated neurons. However, this global coherence could destabilize local activity in the network, particularly self-sustained activity [1]. The precise interplay between local self-sustained activity and global oscillations remains poorly understood and requires further investigation.

Here, we explored the generation of intrinsic oscillation in attractor networks using mean-field models [37]. On the basis of neural circuits underlying working memory and grid cell functioning [1, 38, 39], two kinds of attractor networks (AN-I and AN-II) were developed. The dependence of self-sustained and oscillatory activity on network connectivity, synaptic receptor types, and external input was examined systematically through bifurcation analysis. The distinct dynamics and performances of the AN-I and AN-II were highlighted. This study reveals the general mechanisms for self-sustained activity and oscillatory behavior in attractor networks and offers a framework for investigating similar mechanisms across brain regions.

2 Methodology

2.1 Network connectivity

To elucidate the fundamental mechanisms underlying self-sustained and oscillatory activity, we focused on two attractor networks: one modeling working memory and the other modeling grid cell activity. In the WM network, excitatory principal cells and inhibitory interneurons are uniformly arranged on a separate ring, labeled by angular positions (Fig. 1a), with local excitation among principal cells, uniform excitation

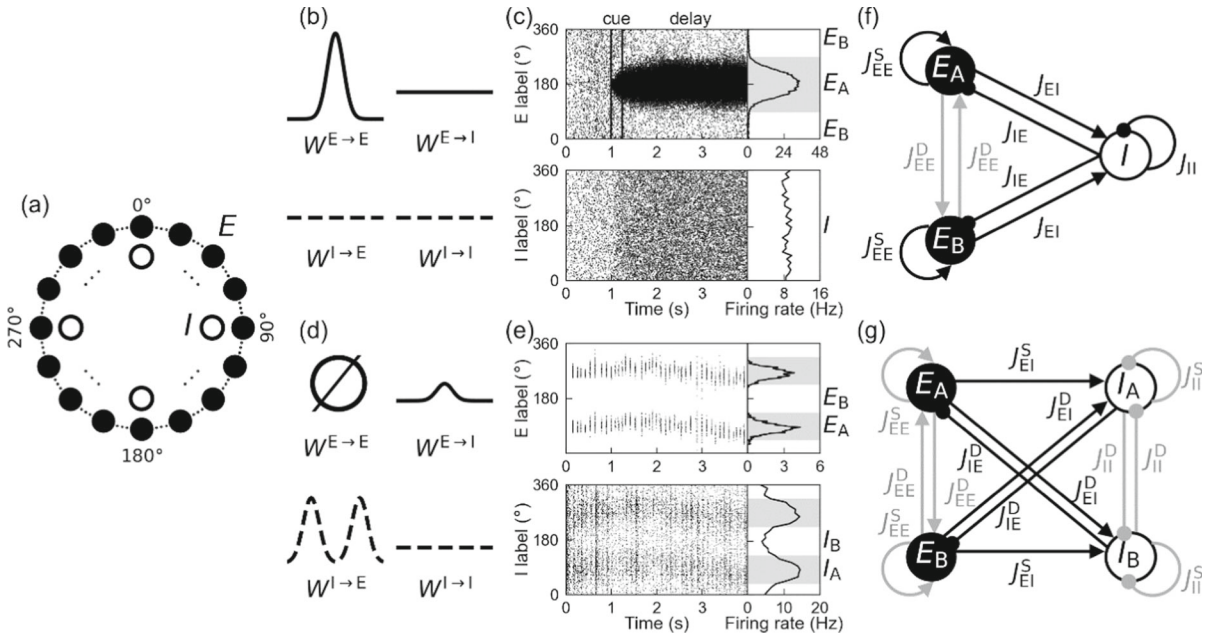

Fig. 1 The continuous and discrete attractor network models for WM and GC dynamics. **a** Network architecture for the continuous attractor network. Excitatory principal cells (solid circles) and interneurons (open circles) are uniformly located on a separate ring and labeled by their angular positions. **b** and **d** Profiles of synaptic connectivity within the WM network (**b**) and GC network (**d**). **c** and **e** Spiking activity of all neurons in the WM network (**c**) and GC network (**e**). Right panels illustrate the mean firing rates averaged over 1.5–2.5 s in the raster plots. The panels reproduce results reported in Refs. [38, 39]. **f** and **g** Schematics of the network connectivity for AN-I (**f**) and AN-II (**g**). Connections depicted in black and gray indicate their inclusion or exclusion in the default models, respectively. Triangular and circular arrowheads separately denote excitatory and inhibitory projections

from principal cells to interneurons, and uniform inhibition among interneurons and from interneurons to principal cells (Fig. 1b) [38]. This network configuration establishes a self-excitation mechanism, leading to persistent firing within a subpopulation of principal cells after cue stimulus removal, spontaneous activity in other principal cells, and uniform firing of interneurons. Notably, the WM network demonstrates spontaneous activity before cue presentation (Fig. 1c).

For direct comparison with the WM network, a biologically realistic torus manifold model was simplified to create a GC-like ring manifold network [39]. Principal cells are also uniformly distributed by angular positions, but direct excitation between them is typically absent. Instead, principal cells excite local interneurons, while interneurons inhibit one another uniformly and deliver structured inhibition to principal cells (Fig. 1d) [39]. This arrangement establishes a self-disinhibition mechanism, allowing local principal cells to sustain persistent firing while the remaining display spontaneous activity (Fig. 1e). Additionally, interneurons exhibit self-sustained activity within localized subsets.

These continuous attractor network (CAN) models offer a biologically plausible framework for understanding neural computation, but their inherent complexity often hinders analytical investigation of core dynamic principles [39, 40]. To identify the essential components driving network behavior, we simplified the CANs into discrete attractor networks (DANs) based on activity patterns and synaptic connectivity profiles. First, despite the translational symmetry of the CANs, which allows self-sustained activity to stabilize at any location on the ring, distinct neuronal subpopulations can be identified based on their activation patterns in stable states [39]. In the WM network, principal cells centered around or distant from the core of self-sustained activity are labeled as populations E_A and E_B, respectively; all interneurons are collectively labeled as the population I (Fig. 1c) [1, 37]. Given the periodic and highly synchronous

nature of the two bump attractors in the GC network, we analyzed the activity of only half of the principal cells and interneurons. Thus, two excitatory populations, E_A and E_B, are defined similarly to the WM network, while interneurons are categorized as I_A and I_B based on their proximity to the core of self-sustained activity (Fig. 1e) [37, 39].

Second, synaptic connectivity between these populations is also simplified. In the WM network, local excitation within each excitatory population is maintained, while cross-excitation between populations is minimal or absent; connections between excitatory and inhibitory populations and self-inhibition are retained (Fig. 1f). In the GC network, direct excitation between principal cells is absent; local excitation from principal cells to interneurons requires that the excitation from E_A to I_A (or E_B to I_B) is much stronger than that from E_A to I_B (or E_B to I_A). Structured inhibition from interneurons to principal cells is implemented, with inhibitory populations targeting excitatory populations with different labels, i.e., I_B (I_A) inhibits E_A (E_B) (Fig. 1g). Uniform inhibition within/between interneuron populations is included when required.

Conclusively, two minimal models were constructed to approximate the dynamics of the CANs. The AN-I model, representing the WM network, comprises two excitatory populations (E_A and E_B) and one inhibitory population (I), while the AN-II model, representing the GC network, consists of two excitatory (E_A and E_B) and two inhibitory (I_A and I_B) populations [1, 37, 39]. In their default configurations, the synaptic connectivity in AN-I includes recurrent connections within and between excitatory and inhibitory populations, while the synaptic connectivity in AN-II is limited to reciprocal connections between excitatory and inhibitory populations. Additional synaptic connections can be incorporated as required to explore specific network dynamics. Simplifying the CANs into DANs enables us to gain deeper insights into the underlying mechanisms of neural dynamics.

2.2 Mean-field models

To comprehensively understand rhythmic activity in attractor networks, a mean-field (MF) modeling approach was employed here [37]. While biophysically realistic models offer a detailed account of neuronal dynamics, the MF framework provides a suitable balance between biological realism and computational efficiency, enabling a systematic investigation of network behavior. In the MF model, the evolution of each population activity is described by

$$\tau_\alpha \frac{dr_\alpha^\beta}{dt} = -r_\alpha^\beta + \varphi_\alpha\left(I_\alpha^\beta\right) \tag{1}$$

where $\alpha = E$ for excitatory principal cells or I for inhibitory interneurons, $\beta = A, B$ or none for population index, r_α^β represents the mean firing rate of each population, and τ_α is the characteristic time constant (set to 10 ms by default). I_α^β is the total synaptic current received, and φ_α is the activation function [41]:

$$\varphi_\alpha\left(I_\alpha^\beta\right) = \frac{c_\alpha I_\alpha^\beta - I_\alpha}{1 - \exp\left(-g_\alpha\left(c_\alpha I_\alpha^\beta - I_\alpha\right)\right)} \tag{2}$$

where c_α, I_α, g_α are constants. For principal cells, $c_E = 310\ (\mathrm{VnC})^{-1}$, $I_E = 125$ Hz, and $g_E = 0.16$ s; for interneurons, $c_I = 615\ (\mathrm{VnC})^{-1}$, $I_I = 177$ Hz, and $g_I = 0.087$ s.

The excitatory synaptic currents are mediated by NMDA receptors (NMDARs) and AMPA receptors (AMPARs), while the inhibitory currents are mediated by $GABA_A$ receptors ($GABA_A$Rs) [36, 42]. The corresponding synaptic gating variables, s_N^β, s_A^β and s_G^β, represent the fraction of receptors in the open state, following different dynamics [37]:

$$\frac{ds_N^\beta}{dt} = -\frac{s_N^\beta}{\tau_N} + \left(1 - s_N^\beta\right)\gamma r_E^\beta \tag{3}$$

$$\frac{ds_A^\beta}{dt} = -\frac{s_A^\beta}{\tau_A} + r_E^\beta \tag{4}$$

$$\frac{ds_G^\beta}{dt} = -\frac{s_G^\beta}{\tau_G} + r_I^\beta \tag{5}$$

where $\tau_N = 100$ ms, $\tau_A = 2$ ms, and $\tau_G = 10$ ms are the characteristic time constants, and $\gamma = 0.641$ is a constant.

Neurons receive recurrent currents and background input; for AN-I,

$$\begin{aligned} I_E^\beta &= J_{EE}^S\left(f_N s_N^\beta + f_A s_A^\beta\right) + J_{EE}^D\left(f_N s_N^{\sim\beta} + f_A s_A^{\sim\beta}\right) - J_{IE} s_G + I_{B\to E} \\ I_I &= J_{EI}\left(f_N s_N^\beta + f_A s_A^\beta\right) + J_{EI}\left(f_N s_N^{\sim\beta} + f_A s_A^{\sim\beta}\right) - J_{II} s_G + I_{B\to I}, \end{aligned} \tag{6}$$

and for AN-II,

$$I_{\alpha}^{\beta} = J_{E\alpha}^{S}\left(f_N s_N^{\beta} + f_A s_A^{\beta}\right) + J_{E\alpha}^{D}\left(f_N s_N^{\sim\beta} + f_A s_A^{\sim\beta}\right) - J_{I\alpha}^{S} s_G^{\beta} - J_{I\alpha}^{D} s_G^{\sim\beta} + I_{B\to\alpha} \quad (7)$$

where $\sim$ labels choosing the opposing neural population. J represents the synaptic strength, which is positive and measured in units of current. The sign $\pm$ denotes whether the connection is excitatory or inhibitory. The contributions of NMDARs and AMPARs to excitatory currents are scaled by f_N and f_A, respectively. By default, $f_N = 1$ and $f_A = 0$, meaning that NMDARs are solely responsible for excitatory transmission. $I_{B\to E}$ and $I_{B\to I}$ represent the excitatory background current to principal cells and interneurons, respectively. $I_{B\to E} = 0.30$ nA and $I_{B\to I} = 0.18$ nA for AN-I; $I_{B\to E} = 0.54$ nA and $I_{B\to I} = 0.18$ nA for AN-II.

In simulations involving stochasticity, all populations receive external noise currents mimicking the stochasticity in ionic channels and synapses, described by the Ornstein–Uhlenbeck process [37, 43]:

$$\tau_{Noise}\frac{dI_{\alpha,Noise}^{\beta}(t)}{dt} = -I_{\alpha,Noise}^{\beta}(t) + \eta_{Noise}\sqrt{\tau_{Noise}}n_{\alpha}^{\beta}(t) \quad (8)$$

where $n_{\alpha}^{\beta}(t)$ is Gaussian white noise with zero mean and unit standard deviation, $\eta_{\mathrm{Noise}} = 0.002$ nA and $\tau_{\mathrm{Noise}} = 0.01$ s are the standard deviation and time constant of the noise current, respectively.

2.3 Numerical method

Unless explicitly specified, parameters assume their default values (Table 1). Neuron parameters were adapted from Ref. [37], and synaptic weights were tuned to ensure self-excitation and self-disinhibition within biologically plausible ranges. Bifurcation analysis was conducted using XPPAUT. Typically, one-parameter bifurcation analysis begins with identifying a fixed point representing the identical activation of E_A and E_B within the explored parameter range; this fixed point serves as the starting point for the analysis, where the value of a single parameter is systematically increased or decreased. If a fixed point cannot be easily identified and only a limit cycle exists, the unstable focus encircled by the limit cycle is used as the starting point. Moreover, to identify potentially missed fixed points, two-parameter bifurcation analysis in the x–y plane is followed by additional one-parameter bifurcation analyses, each with a fixed value of x or y.

Table 1 Default values of synaptic connectivity strength in AN-I and AN-II

AN-I		AN-II	
Parameter	Value	Parameter	Value
J_{EE}^{S}	1.6 nA	J_{EE}^{S}	0 nA
J_{EE}^{D}	0 nA	J_{EE}^{D}	0 nA
J_{EI}	1.0 nA	J_{EI}^{S}	1.5 nA
J_{IE}	1.0 nA	J_{EI}^{D}	1.0 nA
J_{II}	0.2 nA	J_{IE}^{S}	0 nA
		J_{IE}^{D}	1.0 nA
		J_{II}^{S}	0 nA
		J_{II}^{D}	0 nA

Parameters for each example dynamics were selected following the bifurcation analysis. The ordinary differential equations (ODEs) were numerically solved using a fourth-order Runge–Kutta algorithm, with a timestep of 0.02 ms. All variables were initially set to zero, and thus E_A and E_B had the same initial conditions; transient dynamics were discarded when depicting the temporal evolution of variables. Thus, each simulation was initiated from a fixed point or a limit cycle, both characterized by identically activated E_A and E_B.

3 Results

3.1 Mechanisms for the self-sustained and rhythmic activity in AN-I

States of the MF model for ANs can be identified along three dimensions. First, based on activation of E_A and E_B, two states are defined: an identical state, where E_A and E_B are equally activated, and a self-sustained state, where E_A or E_B exhibits persistently stronger activity. Second, states can be stationary or oscillatory based on the presence of oscillations. Third, the stability of each state is classified: a stable state is robust against external disturbance, while an unstable state is easily disrupted. In simulations, E_A and E_B are of the same initial conditions, leading to the identical state, which can be either stable or unstable (Figs. 2a and 3a). To

examine the stability of the identical state and emergence of self-sustained activity, a constant excitatory current is applied exclusively to E_A for 1 s. If a small current disrupts the identical state, causing E_A to exhibit persistently stronger activity than E_B, the identical state is unstable (e.g., types γ, δ, ε in Fig. 2a and η in Fig. 3a). Conversely, if a large current fails to disrupt the identical state, the state is deemed stable (e.g., α in Fig. 2a and θ in Fig. 3a). If the identical state persists under weak disturbance but transitions to the self-sustained state under strong disturbance, both the states are stable (e.g., β in Fig. 2a and λ in Fig. 4e). Both identical and self-sustained states can exhibit oscillatory behavior. Table 2 provides an overview of all state types in AN-I and AN-II, which will be analyzed in detail in the following.

The AN-I exhibits diverse dynamics with varying parameter values. For example, four types of dynamics arise sequentially with increasing the coupling strength of self-excitation $\left(J_{EE}^{S}\right)$. At $J_{EE}^{S} = 1.1$ nA, there exists a single stable stationary identical state (called type α; Fig. 2a). At $J_{EE}^{S} = 1.15$ nA, the network remains in a stable stationary identical (β_0) or self-sustained state (β_1) for different input strengths. This scenario is considered to underlie WM [1]; the identical state represents the spontaneous brain state, while the self-sustained state corresponds to the

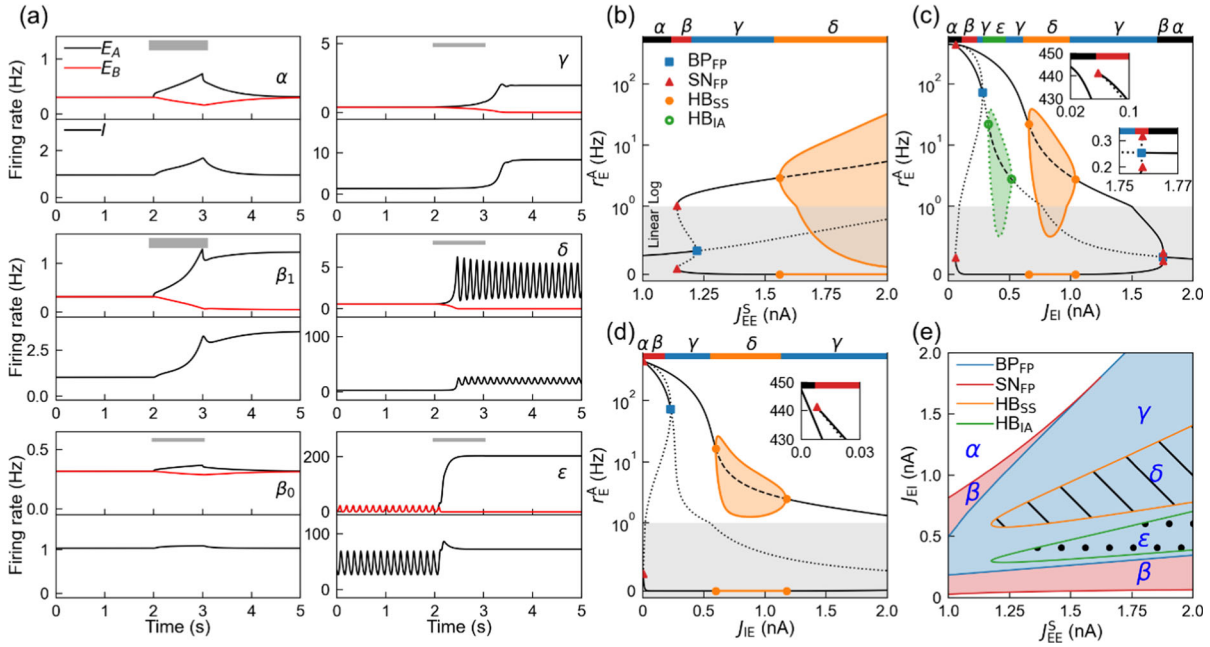

Fig. 2 Population dynamics in AN-I depending on specific synaptic connectivity. **a** Shown are five types of network dynamics, denoted by Greek letters. Gray bars indicate periods of external stimulation applied to the excitatory population E_A, with thicker bars representing a 5-pA stimulus and thinner bars a 1-pA stimulus. Each panel depicts the temporal evolution of firing rates for excitatory populations E_A and E_B (upper) and the inhibitory population I (lower). **b**-**d** Bifurcation diagrams of the firing rate of E_A versus J_{EE}^{S}(**b**), J_{EI} (**c**), and J_{IE} (**d**). Black solid, dashed, and dotted lines represent stable nodes, unstable foci, and unstable saddle points, respectively. Green dotted and orange solid lines delineate the bounds of unstable and stable limit cycles for the identical and self-sustained states, respectively. Bifurcation points are marked by colored symbols: blue squares, red triangles, orange circles, and green circles separately label the pitchfork bifurcation of fixed points (BP_{FP}), saddle-node bifurcation of fixed points (SN_{FP}), Hopf bifurcation on the self-sustained state (HB_{SS}), and Hopf bifurcation on the identical state (HB_{IA}). Bars at the top of each panel in different colors indicate the parameter range for distinct types, with the start and end points of each bar marking bifurcation points. To enhance visualization of extreme E_A rates, log and linear scales are employed in designated regions. Enlarged views of SN_{FP} in **c** and **d** are provided as insets. **e** Two-parameter bifurcation diagram in the $J_{EE}^{S} - J_{EI}$ plane. Blue, red, orange, and green lines represent loci of BP_{FP}, SN_{FP}, HB_{SS}, and HB_{IA} points, respectively. Blue and red areas separately indicate parameter regimes exhibiting bistability and tristability. Hatched and dotted patterns signify parameter regions associated with oscillations in the self-sustained and identical states, respectively

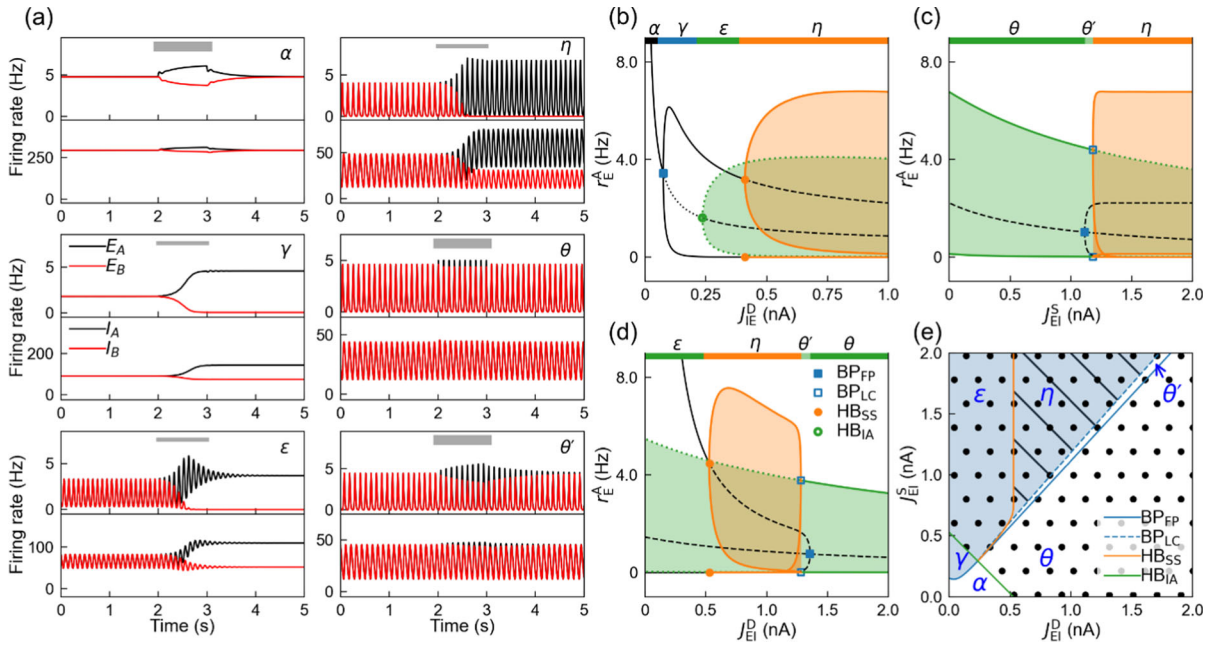

Fig. 3 Population dynamics in AN-II depending on specific synaptic connectivity. **a** Shown are six types of network dynamics, denoted by Greek letters. **b-d** One-parameter bifurcation analysis shows how the firing rate of E_A varies with J_{IE}^D (**b**), J_{EI}^S(**c**), and J_{EI}^D (**d**). **e** Two-parameter bifurcation diagram in the $J_{EI}^S - J_{EI}^D$ plane. Visual elements and their corresponding interpretations are consistent with those described in Fig. 2, with the following additions: green solid lines represent the boundaries of stable limit cycles for the identical state, blue open squares mark pitchfork bifurcations of limit cycles (BP_{LC}), and a blue dashed line in **e** consists of BP_{LC} points

storage of mnemonic items. At $J_{EE}^S = 1.3$ nA, there appears an unstable stationary identical state and a stable stationary self-sustained state (γ). At $J_{EE}^S = 1.6$ nA, the unstable identical state remains stationary, while the self-sustained state exhibits stable oscillations at 7.78 Hz (δ); r_E^A and r_E^B undergo oscillations at high and low activation, respectively. Another type ε emerges by varying the E-to-I coupling strength (J_{EI}); at J_{EI} = 0.4 nA, the unstable identical state exhibits an oscillation of 7.38 Hz, while the stable self-sustained state remains stationary. Meanwhile, the interneuron population tracks the excitatory populations, exhibiting stationary or oscillatory behavior, and is more active when the excitatory populations are in the self-sustained state.

We then explored the mechanisms underlying self-sustained and oscillatory activity in AN-I and their robustness through bifurcation analysis. Considering the importance of self-excitation for sustained activity and negative feedback for oscillation, the analysis focuses on parameters J_{EE}^S, J_{EI}, and J_{IE} (I-to-E coupling strength). The transitions between different types—α to β, β to γ, γ to δ, and γ to ε — correspond to distinct bifurcation types: saddle-node bifurcation of fixed points (SN_{FP}), subcritical pitchfork bifurcation of fixed points (BP_{FP}), Hopf bifurcation on the self-sustained state (HB_{SS}), and Hopf bifurcation on the identically activated state (HB_{IA}), respectively (Fig. 2b-d). In terms of the number of stable states, type β exhibits tristability, while types γ, δ, and ε exhibit bistability. The persistence of memory representation in WM is supported by the presence of self-sustained activity in types β, γ, δ, and ε; particularly, the stable identical state in type β aligns with the spontaneous firing observed in classic CAN models of WM [1].

Self-sustained activity is driven by the self-excitation of E_A (influenced by J_{EE}^S) and is tuned by the negative feedback mediated by J_{EI} and J_{IE}. Insufficient self-excitation disrupts this balance, leading to the collapse of the self-sustained state (Fig. 2b). Weak feedback inhibition fails to adequately suppress E_B, leading to the identical state and overactivation of all populations (Fig. 2c, d), whereas excessive inhibition

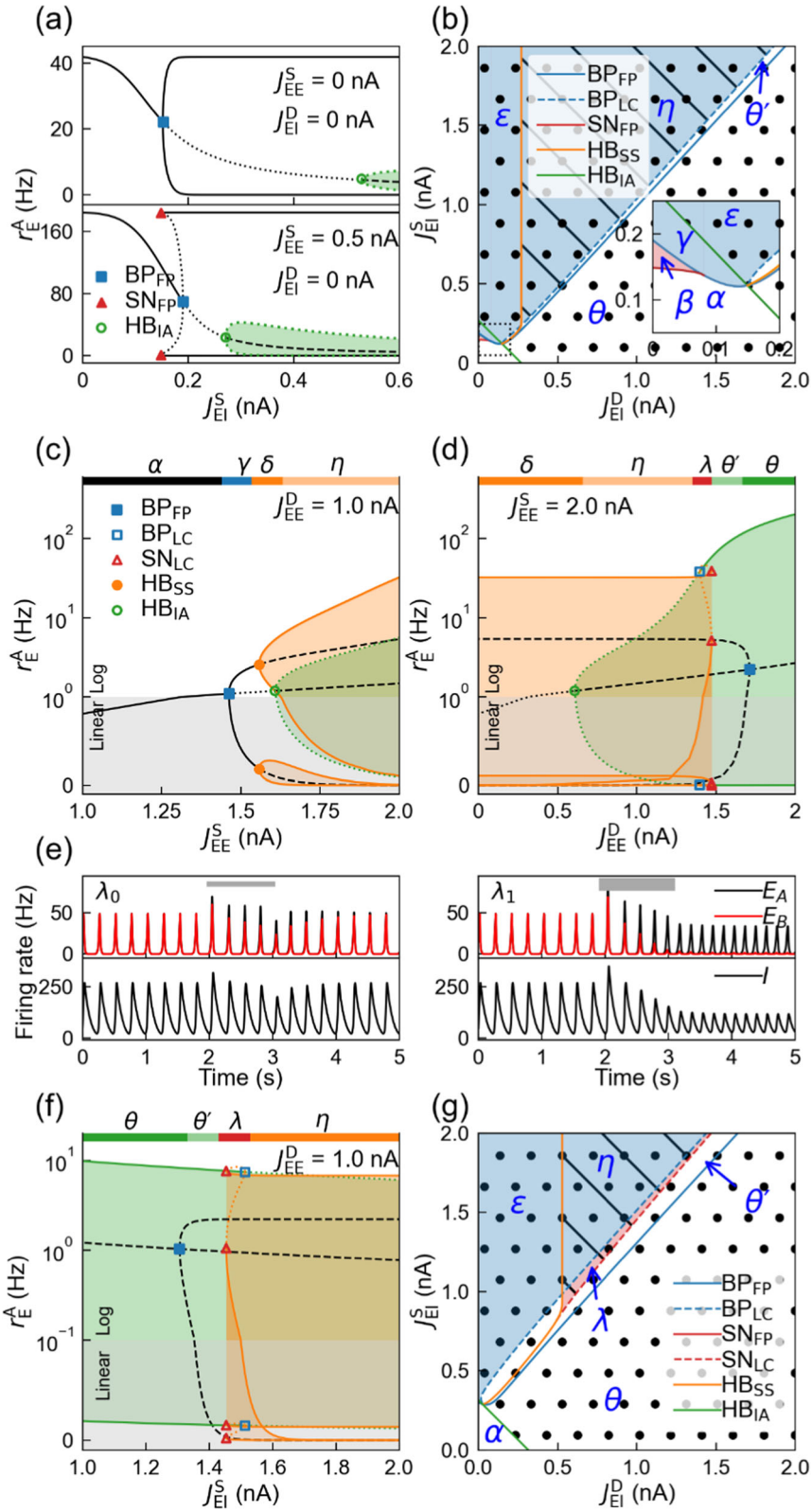

Fig. 4 Excitation of principal cell populations modulating the network dynamics. **a** and **b** Influence of self-excitation on AN-II dynamics. **a** Bifurcation diagrams of r_E^A versus J_{EI}^S for $J_{EE}^S = 0$ (upper) or 0.5 nA (lower). **b** Two-parameter bifurcation diagram in the $J_{EI}^D - J_{EI}^S$ plane for $J_{EE}^S = 0.5$ nA. An enlarged view of the area enclosed by the dotted square is provided as an inset. **c**-**e** Impact of mutual excitation on AN-I dynamics. Bifurcation diagrams of r_E^A versus J_{EE}^S for $J_{EE}^D = 1$ nA (**c**) and versus J_{EE}^D for $J_{EE}^S = 2$ nA (**d**). **e** Shown are the λ-type dynamics at $J_{EE}^D = 1.44$ nA and $J_{EE}^S = 2.0$ nA, with stimulus periods marked by thick (20 pA) or thin (10 pA) bars. **f** and **g** Combined effects of mutual excitation and self-excitation on AN-II dynamics. **f** Bifurcation diagram of r_E^A versus J_{EI}^S for $J_{EE}^D = 1.0$ nA. **g** Two-parameter bifurcation diagram in the $J_{EI}^D - J_{EI}^S$ plane for $J_{EE}^D = 1$ nA. The notations for symbols, lines, scatters, and areas remain consistent with those in Figs. 2 and 3. Additionally, red open triangles in **d** and **f** denote saddle-node bifurcations of limit cycles (SN_{LC}), and a red dashed line in **g** consists of SN_{LC} points

Table 2 An overview of different states in AN-I and AN-II

Label	State	Oscillation	Stability
α	Identical state	No	Yes
β	Identical state	No	Yes
	Self-sustained state	No	Yes
γ	Identical state	No	No
	Self-sustained state	No	Yes
δ	Identical state	No	No
	Self-sustained state	Yes	Yes
ε	Identical state	Yes	No
	Self-sustained state	No	Yes
η	Identical state	Yes	No
	Self-sustained state	Yes	Yes
θ	Identical state	Yes	Yes
λ	Identical state	Yes	Yes
	Self-sustained state	Yes	Yes

indiscriminately suppresses both E_A and E_B, hindering self-sustained activity altogether. On the other hand, oscillations in the self-sustained state are primarily driven by the negative feedback between activated E_A and I, whereas oscillations in the identical state rely on the combined negative feedback between $E_A + E_B$ and I. The nonlinearity inherent in self-excitation is also crucial for maintaining oscillations. Insufficient self-excitation prevents the establishment of sustained oscillations (Fig. 2b, e). Collectively, the AN-I can maintain self-sustained and rhythmic activity, but these behaviors are highly dependent on parameter settings.

3.2 Mechanisms for the self-sustained and rhythmic activity in AN-II

The AN-II also exhibits a rich repertoire of dynamics with varying parameter values, some of which mirror those observed in AN-I (Fig. 3a). For example, four types of dynamics appear successively with increasing the I-to-E coupling strength $\left(J_{IE}^{D}\right)$; types α, γ, and ε manifest at $J_{IE}^{D} = 0.05$ nA, 0.2 nA, and 0.3 nA, respectively. A new type (η) emerges at $J_{IE}^{D} = 1.0$ nA, where the stable self-sustained and unstable identical states oscillate at 9.93 Hz and 8.95 Hz, respectively. Another type θ arises by varying J_{EI}^{S}; at $J_{EI}^{S} = 1.15$ nA, the only stable identical state oscillates at 9.16 Hz. Intriguingly, types γ, ε, and η are implicated in the maintenance of self-sustained activity observed in grid cells, crucial for spatial navigation [3, 39]. Particularly, oscillations in type η may underlie the accompanying theta rhythm (4–12 Hz) [39].

Given the importance of structured E-to-I connectivity for self-sustained activity and negative feedback for oscillation [39], we performed bifurcation analysis centered on coupling strengths J_{EI}^{S}, J_{EI}^{D}, and J_{IE}^{D}. While the γ to ε transition mirrors that in AN-I through HB_{IA}, other transitions undergo distinct bifurcation types (Fig. 3b). The conversions from α to γ, ε to η, and θ to η correspond to supercritical BP_{FP}, HB_{SS}, and supercritical pitchfork bifurcation of limit cycles (BP_{LC}), respectively. When the network dynamics shift from type θ to η, BP_{LC} consistently follows BP_{FP} (Fig. 3c, d), which results in a new type θ' resembling type θ (Fig. 3a). The persistence of position representation is supported by the presence of self-sustained states in types γ, ε and η; the oscillations observed in the self-sustained state of type η align with the theta oscillations of GCs.

The rich dynamics of AN-II arise from a delicate interplay between excitatory and inhibitory connections. Activated E_A (or E_B) excites I_A (I_B), which in turn inhibits E_B (E_A) to sustain the activity of E_A (E_B); thus, decreasing J_{EI}^{S} or J_{IE}^{D} leads to cessation of self-sustained activity (Fig. 3b, c). Oscillations in the self-sustained state arise through a distinct negative feedback mechanism. Activated E_A also excites I_B, and I_B suppresses E_A; thus, oscillations arise with increasing J_{IE}^{D} or J_{EI}^{D} (Fig. 3b, d). The differential roles of I_A and I_B underscore the importance of structured synaptic connectivity in AN-II's functionality.

For self-sustained activity to be maintained when $J_{EI}^{S} > J_{EI}^{D}$ (Fig. 3e), the inhibition of E_B by I_A ($E_A \rightarrow I_A \dashv E_B$) must be stronger than the inhibition of E_A by I_B ($E_A \rightarrow I_B \dashv E_A$), representing a self-disinhibition mechanism. In contrast, oscillations in the identical state depend on the combined negative feedback between $E_A + E_B$ and $I_A + I_B$. Thus, HB_{IA} arises more readily than HB_{SS} (Fig. 3b, e). Together, the default configuration of AN-II is able to maintain self-sustained and rhythmic activity with a relatively simple dependence on parameters, but unable to exhibit the β-type dynamics.

3.3 Influence of self- and mutual excitation of principal cells on network dynamics

As demonstrated above, the self-sustained activity is achieved through self-excitation in AN-I or self-disinhibition in AN-II. However, recent experimental data from grid cells suggest some residual self-excitation among excitatory neurons [44]. With self-excitation (regulated by J_{EE}^{S}) present in AN-II, the previously observed BP_{FP} becomes subcritical, and an SN_{FP} emerges, resulting in a transition to β-type dynamics (Fig. 4a). Additionally, the enhanced positive feedback leads to a significant increase in E_A activity. The self-excitation expands the parameter range for oscillations in both states due to the enhanced nonlinearity within the network, allowing the onset of oscillation at lower parameter values (Fig. 4a, b). Notably, the disinhibition of E_A remains the primary driver for self-sustained activity, which requires $J_{EI}^{S} > J_{EI}^{D}$. However, the required difference between J_{EI}^{S} and J_{EI}^{D} decreases with the introduction of self-excitation. Together, incorporating the self-excitation allows for β-type dynamics in AN-II and modulates existing states through enhanced nonlinearity.

After exploring the role of self-excitation, we investigated the impact of mutual excitation between E_A and E_B (modulated by J_{EE}^{D}) on AN-I dynamics. This mutual excitation facilitates oscillations in the identical state, resulting in η- or θ-type dynamics (Fig. 4c, d). While increasing J_{EE}^{S} or J_{EE}^{D} promotes the occurrence of HB_{IA}, HB_{SS} remains largely unaffected (Figs. 2b and 4c), indicating that mutual excitation primarily influences the collective dynamics of E_A and E_B rather than their individual behaviors. Furthermore, mutual excitation eliminates β-type dynamics and induces new λ-type dynamics characterized by stable oscillations in both the identical and self-sustained states. At J_{EE}^{D} = 1.44 nA and J_{EE}^{S} = 2.0 nA, for instance, their oscillation frequencies are 5.96 Hz and 3.93 Hz, respectively (Fig. 4e). Transitions from types η to λ and θ to λ involve bifurcations like BP_{LC} and the saddle-node bifurcation of limit cycles (SN_{LC}).

Similarly, mutual excitation in AN-II promotes oscillations in the identical state, leading to the emergence of λ-type dynamics (Fig. 4f); at J_{EE}^{D} = 1.0 nA and J_{EI}^{S} = 1.48 nA, the two oscillation frequencies are 9.70 Hz and 7.03 Hz, respectively. Oscillations in the identical state occur more readily, while those in the self-sustained state remain unaffected, as indicated by the positions of HB_{IA} and HB_{SS} (Figs. 3e and 4g). Overall, mutual excitation between excitatory populations promotes oscillations in the identical state.

3.4 Impact of interneuron mutual inhibition on network dynamics

It has been demonstrated earlier that the inhibition from interneurons to principal cells is crucial for maintaining the self-sustained and oscillatory activity. We further investigated the impact of mutual inhibition between interneurons on network dynamics; without loss of generality, $J_{II}^{S} = J_{II}^{D} = J_{II}$ in AN-II. Despite variations in J_{II} strength, the predominant excitatory population consistently maintains higher activation levels in both AN-I and AN-II (Fig. 5a, b); moreover, r_E^A in the γ-type dynamics rises with increasing J_{II} due to a decrease in overall feedback inhibition. However, oscillatory activity is significantly disrupted by elevating J_{II}. Similar results are observed when J_{II}^{S} and J_{II}^{D} vary independently in AN-II (Fig. 5c). This disruption occurs because strong mutual inhibition dampens the response of interneurons to principal cell activity; consequently, increasing J_{II} weakens the negative feedback between principal cells and interneurons, essential for generating oscillations. Collectively, enhancing interneuron mutual inhibition has opposing effects on network dynamics; while self-sustained activity remains relatively robust, oscillatory dynamics are highly sensitive to this form of inhibition.

3.5 Differential roles of NMDARs and AMPARs in AN-I and AN-II dynamics

Beyond the network connectivity, receptor subtypes play a pivotal role in shaping network dynamics. Previous studies have highlighted the importance of NMDARs for self-sustained activity and AMPARs for oscillatory behavior [1, 35]. The scaling factors f_N and f_A are set to default values of 1.0 and 0.0, respectively, indicating a full predominance of NMDARs. Here, we systematically varied f_N and f_A to investigate their influence on network dynamics.

In AN-I, decreasing f_N at f_A = 0 leads to a sequence of bifurcations (inverse HB_{SS}, BP_{FP}, and SN_{FP}) and

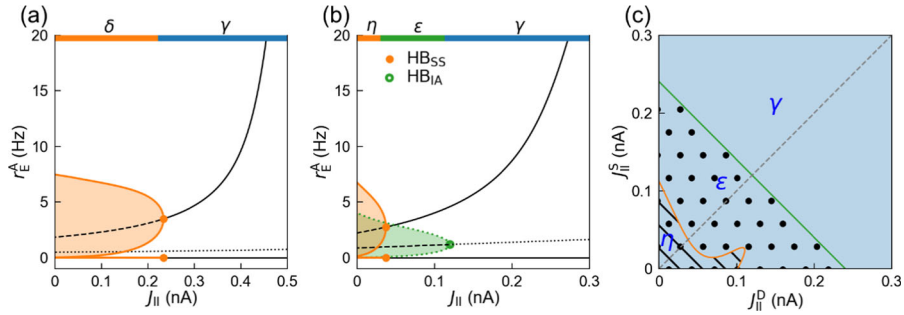

Fig. 5 Impact of interneuron mutual inhibition on network dynamics. **a** and **b** Bifurcation diagrams of r_E^A versus J_{II} for AN-I (**a**) and AN-II (**b**). **c** Two-parameter bifurcation diagram in the $J_{II}^D - J_{II}^S$ plane for AN-II. The interpretation of lines, scatters, areas, and symbols remains consistent with Fig. 2

dynamic transitions from δ to γ, β, and finally α (Fig. 6a), demonstrating the influence of NMDAR activity on both self-sustained and oscillatory activity. At $f_N = 0.6$ nA, increasing f_A results in the occurrence of subcritical BP_{FP} and HB_{SS} and transitions from β to γ and δ (Fig. 6b). While the self-sustained state is always maintained, the identical state can vary in stability, suggesting that AMPAR activity primarily modulates the oscillatory behavior of the self-sustained state. Furthermore, self-sustained oscillations emerge at higher f_A values when f_N is reduced. These distinct effects of f_N and f_A on network dynamics are primarily due to the different time constants of NMDAR and AMPAR currents. The slower NMDAR kinetics allow for prolonged temporal integration of synaptic inputs, which is crucial for reverberatory

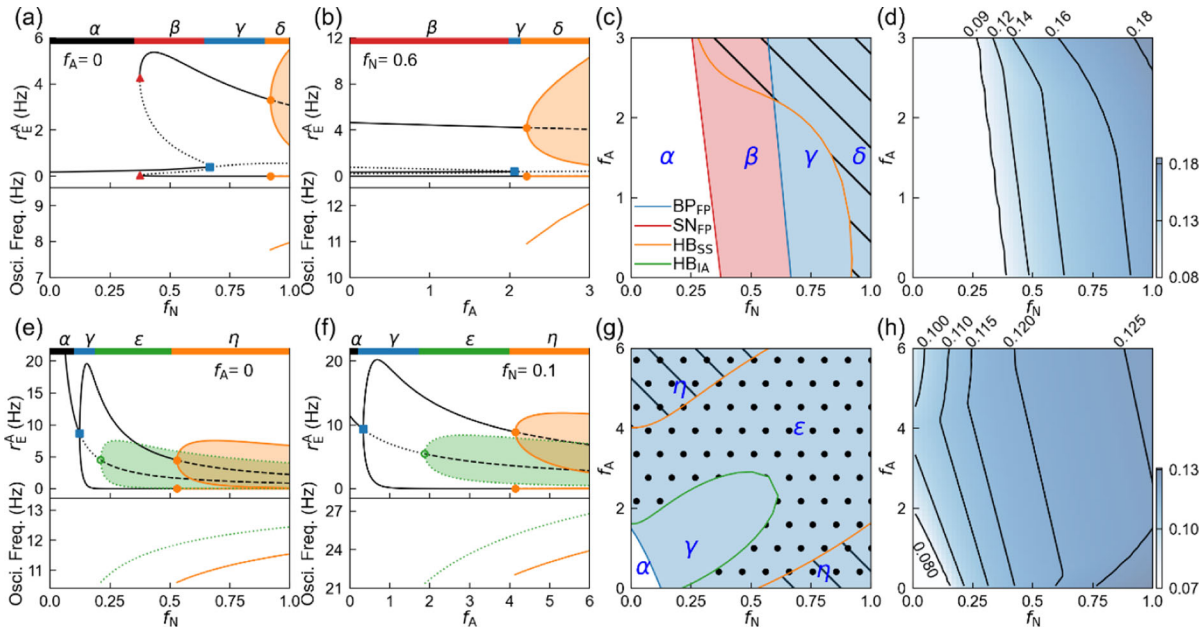

Fig. 6 Dependence of network dynamics on f_A and f_N. **a**-**d** and **e**–**h** correspond to the AN-I and AN-II, respectively. Bifurcation diagrams for the variation of r_E^A with f_N at $f_A = 0$ (**a**), with f_A at $f_N = 0.6$ (**b**), with f_N at $f_A = 0$ (**e**), and with f_A at $f_N = 0.1$ (**f**). **c** and **g** Two-parameter bifurcation diagrams in the f_N–f_A plane. The interpretation of lines, scatters, and areas remains consistent with Fig. 2. Lower panels in **a**, **b**, **e** and **f** depict the oscillation frequencies of the self-sustained (orange lines) and identical (green dotted lines) states. **d** and **h** Contour maps of mean excitatory activity during self-sustained states. For each pair of f_N and f_A eliciting self-sustained activity, $f_N s_N^A + f_A s_A^A$ was averaged over a 10-s period, regardless of whether the activity is oscillatory or not. The magnitude is indicated by the blue color scale, with selected contour lines and their associated values displayed. Each map was generated using a 50 × 50 grid of f_N and f_A values, uniformly sampled within the depicted area

activity and slow oscillations, whereas the faster AMPAR kinetics are less effective in sustaining such activity. The two-parameter bifurcation analysis confirms these observations (Fig. 6c). The lines of SN_{FP} and BP_{FP} points are nearly parallel to the f_A axis, indicating the independence of self-sustained activity from f_A. Moreover, the onset of oscillations is advanced with increasing f_A. Notably, the oscillation frequency of self-sustained activity rises with increasing f_N or f_A, falling within the theta band (4–12 Hz).

By simultaneously varying f_N and f_A, we investigated whether overall excitation or the relative contribution of NMDAR and AMPAR currents dominates network dynamics. We visualized the average of overall excitation $\left(f_N s_N^A + f_A s_A^A\right)$ over a 10-s window, s^A, during self-sustained states on the f_N–f_A plane using a contour map (Fig. 6d). s^A rises more prominently with increasing f_N than with f_A, indicating that NMDAR currents contribute more significantly to overall excitation than AMPAR currents. Along a given contour line, the value of s^A remains constant, while the relative NMDAR/AMPAR contribution varies. If a contour line intersects a line of bifurcation points, the bifurcation arises due to changes in the relative NMDAR/AMPAR contribution. If a contour line parallels a line of bifurcation points, the bifurcation arises due to changes in overall excitation. The lines of SN_{FP} and BP_{FP} points largely parallel the contour lines, suggesting that these bifurcations occur primarily due to changes in overall excitation, demonstrating the dominance of overall excitation on self-sustained activity. The modulation of oscillatory activity is more complex. At lower f_A and higher f_N values, the HB_{SS} occurs along lines perpendicular to the excitation contours, demonstrating the dominant role of overall excitation. At higher f_A and lower f_N values, the HB_{SS} can be influenced by both overall excitation and the relative NMDAR/AMPAR contribution, as indicated by the $\sim 45°$ angle between the contour lines and the line of HB_{SS} points. Together, NMDAR currents play a more crucial role in shaping network dynamics, especially self-sustained activity, likely due to their longer time constants.

In AN-II, decreasing f_N at $f_A = 0$ results in a sequential progression through types η, ε, γ, and α (Fig. 6e). For $f_N = 0.1$, the network exhibits low-gamma oscillations at $f_A = 6.0$, with the self-sustained and identical states in type η oscillating at 23.90 Hz and 26.78 Hz, respectively, in contrast to theta oscillations generated under high f_N; this discrepancy stems from the faster kinetics of AMPARs-medicated currents ($\tau_A = 2$ ms) compared to NMDARs ($\tau_N = 100$ ms). Reducing f_A yields a bifurcation sequence mirroring that in Fig. 6d (Fig. 6f). Thus, the AN-II is capable of self-sustained activity regardless of whether NMDARs or AMPARs dominate synaptic transmission, since the self-disinhibition involves a multi-step mechanism of E_A-I_A-E_B (E_B-I_B-E_A), effectively slowing down the interaction, compared to the direct self-excitation of E_A (E_B) in AN-I. Oscillatory activity emerges with high f_N or f_A (Fig. 6g) but exhibits distinct frequency characteristics: theta oscillations with dominant NMDARs, or low-gamma oscillations with dominant AMPARs (see lower panels in Fig. 6e, f). Similarly, NMDARs contribute more significantly to overall excitation than AMPARs (Fig. 6h). Overall excitation predominantly governs self-sustained activity and NMDAR-dominated oscillations, while the relative NMDAR/AMPAR contribution markedly influences AMPAR-dominated oscillations. This is reflected in the orientation of excitation contour lines: they are parallel to the lines of BP_{FP} and HB_{SS} points at large f_N but perpendicular to the line of HB_{SS} points at large f_A. These results underscore the intricate interplay between receptor subtypes in modulating the functional dynamics of ANs.

3.6 Noise-driven rhythmic bursting

Here, we separately varied background excitatory currents and introduced noise perturbations [38, 39] to explore their impact on network dynamics. In AN-I and AN-II, increasing the excitatory drive to principal cells promotes the emergence of self-sustained and oscillatory activity, while a moderate input to interneurons facilitates the onset of oscillations. In AN-I, increasing $I_{B\to E}$ sequentially triggers SN_{FP}, BP_{FP}, HB_{SS}, and HB_{IA}, transitioning network dynamics from α to β, γ, δ and η regimes (Fig. 7a); in AN-II, BP_{FP}, HB_{IA}, and HB_{SS} appear sequentially, leading to similar transitions from α to γ, ε, and η (Fig. 7c). Thus, sustained activation of the principal cell population requires sufficient excitatory input besides recurrent synaptic currents.

Similarly, decreasing $I_{B\to I}$ in AN-I results in the sequential emergence of BP_{FP}, HB_{SS}, and HB_{IA}, with the network transitioning through α, γ, δ, and η dynamics (Fig. 7b); in AN-II, BP_{FP}, HB_{IA}, and HB_{SS}

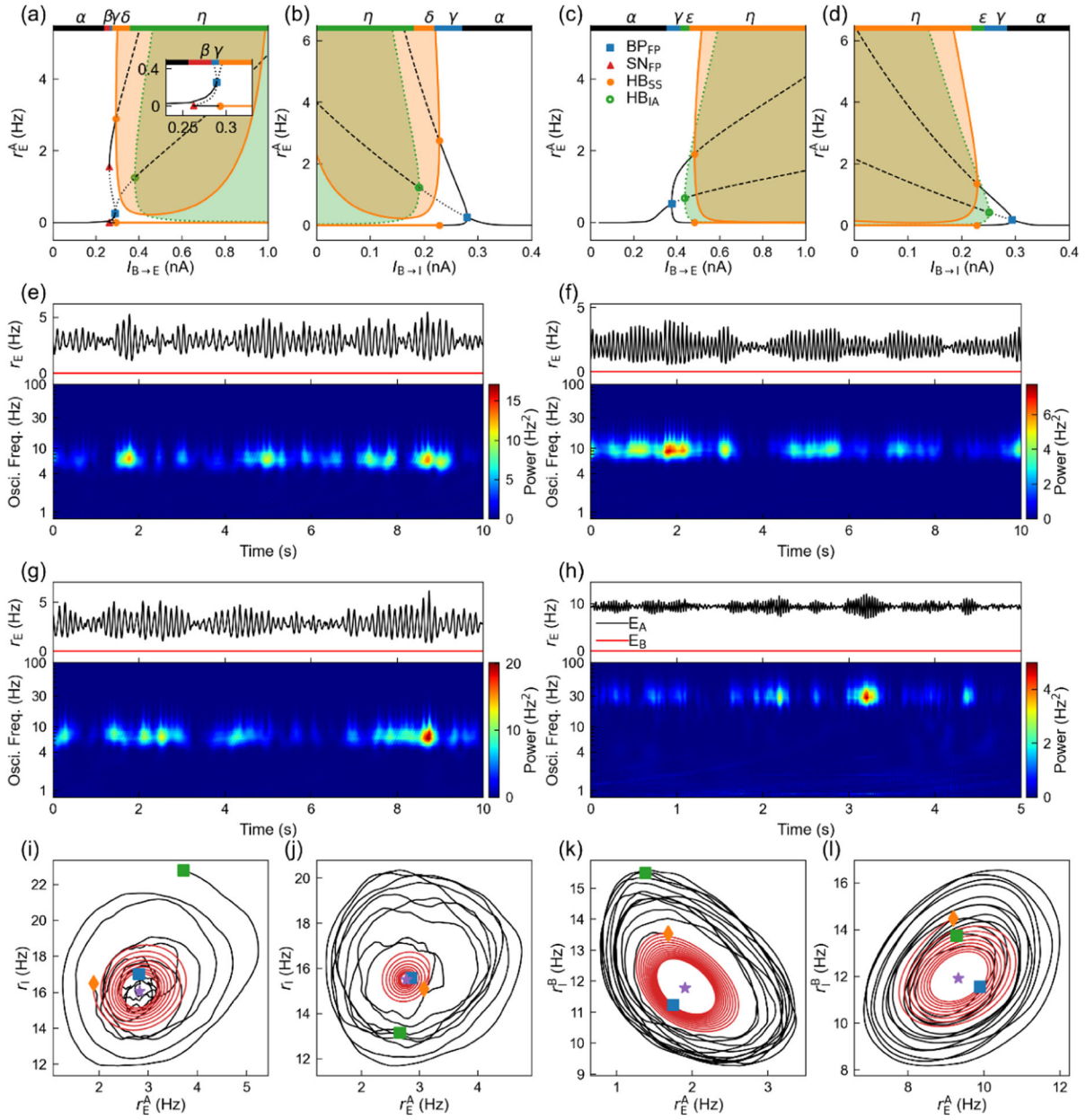

Fig. 7 Impact of background input and noise on network dynamics. **a**-**d** One-parameter bifurcation analysis illustrates how r_E^A varies with $I_{B\to E}$ (**a**) and $I_{B\to I}$ (**b**) in AN-I, and with $I_{B\to E}$ (**c**) and $I_{B\to I}$ (**d**) in AN-II. The interpretation of lines, scatters, and areas aligns with Fig. 2. An enlarged view of SN_{FP} in **a** is provided as an inset. **e**–**h** Temporal evolution of r_E^A(black) and r_E^B(red, upper) and the corresponding power spectrum analysis (color coded; lower) for $I_{B\to E} = 0.29$ nA in AN-I (**e**), $I_{B\to E} = 0.48$ nA in AN-II (**f**), $J_{EE}^S = 1.52$ nA in AN-I (**g**), and $f_A = 3.85$ and $f_N = 0.1$ in AN-II (**h**). **i**-**l** Representative traces (black lines) in the $r_E^A - r_I$ (for AN-I) or $r_E^A - r_E^B$ (for AN-II) phase plane, separately corresponding to time windows in **e**–**h**: **e** (0.6–1.8 s), **g** (3.5–4.0 s), **f** (4.5–5.7 s), and **h** (3–3.4 s). For comparison, traces from deterministic simulations (red lines) are included, all initiated from the same initial condition. Purple stars, orange diamonds, green squares, and blue squares denote the stable foci, initial points, endpoints of stochastic and deterministic traces, respectively

occur sequentially, transforming network dynamics from α to γ, ε, and η (Fig. 7d). Excessive interneuron activation (under high $I_{B\to I}$) inhibits all principal cells indiscriminately in both networks, leading to the suppression of self-sustained and oscillatory activity. Together, adequate excitatory input to principal cells combined with moderate input to interneurons promotes self-sustained and oscillatory activity in both networks.

Recent arguments against attractor network models of working memory have arisen from observations of bursting oscillations during the delay period, suggesting an absence of stable persistent activity [15, 21]. Here, we investigated the mechanism of noise-driven rhythmic bursting that may underlie those observations. When $I_{B\to E}$ is slightly lower than that at HB_{SS}, both networks remain in the stable stationary state in the absence of noise (Fig. 7a-d). The introduction of noise can induce transient oscillatory bursts, characterized by brief deviations from the stationary state followed by a return (Fig. 7e, f). In fact, these bursts are observed across a range of parameter values, but burst frequencies predominantly reside within the theta range for AN-I and span the theta to low-gamma bands for AN-II (Fig. 7g, h). The rhythmic bursting can be understood as follows. With parameter values marginally lower than those at HB_{SS}, the fixed points are stable foci, and the network spirals toward these foci from an unstable initial condition in deterministic cases (Fig. 7i-l). In the presence of noise, however, the network can be transiently displaced far from the foci, effectively prolonging the time taken to reach them and resulting in rhythmic bursts. Noise can elicit oscillatory activity in networks operating near bifurcation points, highlighting its role in modulating neural dynamics [45].

4 Discussion

We investigated the mechanisms for intrinsic oscillations in two types of attractor networks. Although self-sustained activity is maintained through self-excitation in AN-I and self-disinhibition in AN-II, oscillations in both networks arise from negative feedback interactions. Oscillations in the self-sustained state arise from negative feedback between activated principal cells and interneurons, whereas oscillations in the identical state result from negative feedback between the entire excitatory and inhibitory populations. Furthermore, the intricate interactions between neural populations and the dynamics of synaptic currents introduce the necessary nonlinearity and time delays to sustain oscillations. Consequently, both the AN-I and AN-II exhibit a diverse repertoire of dynamical states across biologically plausible parameter ranges, encompassing types α, β, γ, δ, ε, η, θ, and λ, with similar modulation patterns.

Three key mechanisms are worth noting. First, self-excitation of principal cells facilitates the tristability of stationary states, while mutual excitation between principal populations is critical for the tristability of oscillatory states. Second, excessive inhibition among interneurons can suppress oscillatory activity, preventing sustained oscillations. Third, appropriate levels of background excitation to principal cells and interneurons are necessary to support a variety of dynamical states. These mechanisms can be further examined in more detailed network models comprising spiking neurons. While eight distinct dynamic regimes are possible within this framework, future research is required to determine which specific combinations are relevant to different cognitive processes. The observed transitions between these dynamic regimes suggest potential experimental strategies to explore their functional significance.

While both the AN-I and AN-II demonstrate the capability for self-sustained and oscillatory activity, their underlying mechanisms and robustness differ markedly. Despite its simpler architecture, the AN-I demands more precise parameter tuning, as its single interneuron population supports both dynamics through intricate interactions involving self-excitation, inhibition, and nonlinearity. In contrast, the AN-II benefits from specialized interneuron populations, each contributing to distinct dynamics, allowing for more straightforward parameter modulation and enhanced robustness. These findings highlight the importance of network architecture and interneuron diversity in shaping the dynamics and robustness of neural circuits.

In canonical models, NMDARs primarily support sustained activity, while AMPARs drive oscillations [1, 35], as manifested in AN-I. However, this division of labor is less pronounced in AN-II, where both receptor types contribute to both activity patterns. Notably, NMDARs underpin slower oscillations and AMPARs faster oscillations. The varying contributions of NMDARs and AMPARs to network dynamics may influence the emergence of distinct oscillatory

frequencies, suggesting a correlation between the predominant excitatory receptor type and neural rhythms across different brain regions. This implies that NMDAR-rich and AMPAR-rich regions might favor slower and faster oscillations, respectively.

Intrinsic network stochasticity can induce transient oscillatory bursts even in parameter regimes below the Hopf bifurcation point. Remarkably, self-sustained activity persists during these episodes, albeit with intermittent transitions between stationary and oscillatory states. This phenomenon agrees with the experimental observations, where sparse bursts are detected in individual trials and consistent patterns of persistent spiking emerge when averaged across trials in WM tasks [15, 21]. While noise drives these state fluctuations in our model, synaptic plasticity could potentially regulate this process for adaptive information processing [46–48].

A major limitation of our mean-field models is their lack of saturation, which can lead to unrealistically high firing rates for certain parameter values (e.g., α, β, and ε in Fig. 2c, d). Results in these regimes are interpreted qualitatively, with a focus on overall trends and bifurcations rather than precise firing rates. Importantly, our main conclusions regarding the interplay between self-sustained and oscillatory activity are based on results obtained within biologically plausible firing rate regimes. Future work using networks of spiking neurons, informed by the mechanisms identified here, will provide more quantitatively robust results. Our findings also align with key aspects of previous research using full spiking neuron models [38, 39]. While mean-field models offer computational efficiency and capture essential network dynamics, they inherently average over individual neuronal interactions, potentially missing some behaviors such as phase locking and phase precession [16, 17]. Nevertheless, our results provide valuable insights into the principles governing self-sustained and oscillatory activity in attractor networks. This work establishes a foundation for future studies using more detailed models to validate our conclusions and explore the full spectrum of neural dynamics.

Local networks of excitatory and inhibitory neurons are a common motif in brain circuitry [49, 50]. Our model identifies eight distinct dynamic regimes that could be exploited to characterize the behavior of these local networks. Simulating individual brain areas with our mean-field model allows the construction of larger-scale models encompassing multiple areas, which could be used to explore large-scale oscillatory phenomena, including inter-areal interactions of diverse rhythms, propagation of oscillations, and synchronization across areas [51–53].

Acknowledgements This work was supported by STI 2030—Major Projects 2021ZD0201300 and the Nanjing University Integrated Research Platform of the Ministry of Education—Top Talents Program 2024300464. The numerical calculations in this paper have been performed on the computing facilities at the High Performance Computing Center (HPCC) of Nanjing University.

Author contributions F.L., T.W. and W.W. designed research. T.W. performed research. All authors analyzed the data. T.W. and F.L. wrote the manuscript.

Data availability All data needed to evaluate the conclusions in the paper are present in the paper. Custom python codes will be available upon request to F.L.

Declarations

Competing interest The authors declare no competing interests.

Appendix

To generate Fig. 1c and e, we simulated a network of spiking neurons based on previously developed models [38, 39]. A full description of the model is presented here. The network consists of N_{E} excitatory principal cells (E) and N_{I} inhibitory interneurons (I): $N_{\mathrm{E}} = 2048$ and $N_{\mathrm{I}} = 512$ for AN-I and $N_{\mathrm{E}} = 1024$ and $N_{\mathrm{I}} = 256$ for AN-II. Principal cells and interneurons are uniformly distributed on separate rings, and each neuron is labeled by its angular position θ. All neurons are described by the leaky integrate-and-fire (LIF) model:

$$C_m \frac{dV_m(t)}{dt} = -g_L(V_m(t) - V_L) - I_{syn}(t) + I_{ext}(t) \tag{A1}$$

where V_{m}, C_{m}, g_{L} and V_{L} are the membrane potential, membrane capacitance, leaky conductance, and resting potential, respectively. $I_{\mathrm{syn}}(t)$ is the total recurrent synaptic current. $I_{\mathrm{ext}}(t)$ is the external current, comprising background input, noise current, and the stimulus. When V_{m} reaches the threshold V_{th}, a spike is fired and V_{m} is reset to V_{reset} for a refractory period

τ_{ref}. For principal cells, C_m = 0.5 nF, g_L = 25 nS, V_L = -70 mV, V_{th} = -50 mV, V_{reset} = -60 mV, and τ_{ref} = 2 ms; for interneurons, C_m = 0.2 nF, g_L = 20 nS, V_L = -70 mV, V_{th} = -50 mV, V_{reset} = -60 mV, and τ_{ref} = 1 ms [14].

Neurons receive both excitatory postsynaptic currents (EPSCs) and inhibitory postsynaptic currents (IPSCs), respectively, from pyramidal cells and interneurons. EPSCs are mediated by AMPARs and NMDARs, while IPSCs are mediated by GABARs. The total recurrent synaptic current to neuron i (either pyramidal cell or interneuron) reads

$$I_{i,syn}(t) = I_{i,NMDA}(t) + I_{i,GABA}(t) \tag{A2}$$

with

$$I_{i,NMDA}(t) = \frac{g_{NMDA}\left(V_{i,m}(t) - V_E\right)}{1 + [Mg^{2+}]\exp\left(-0.062V_{i,m}(t)\right)/3.57}\sum_{j=1}^{N_E} W_{ij}S_{j,NMDA} \tag{A3}$$

$$I_{i,GABA}(t) = g_{GABA}\left(V_{i,m}(t) - V_I\right)\sum_{j=1}^{N_I} W_{ij}S_{j,GABA} \tag{A4}$$

where g is the maximum synaptic conductance, V_E = 0 mV and V_I = -70 mV are the reversal potentials of excitatory and inhibitory synapses, and $[Mg^{2+}]$ = 1 mM. The index j runs over all presynaptic neurons, W_{ij} is the connectivity strength, and S_j is the gating variable (i.e., the fraction of receptors in the open state). For AN-I, $g_{NMDA}^{E\to E} = 0.286$, $g_{NMDA}^{E\to I} = 0.219$, $g_{GABA}^{I\to E} = 1.336$, and $g_{GABA}^{I\to I} = 1.024$ (in nS); for AN-II, $g_{NMDA}^{E\to E} = 0.0$, $g_{NMDA}^{E\to I} = 0.4$, $g_{GABA}^{I\to E} = 2.4$, and, $g_{GABA}^{I\to I} = 0.04$ (in nS).

Given a spike train $\{t_k\}_j$ in the presynaptic neuron j, $S_{j,GABA}$ follows the first-order dynamics:

$$\frac{dS_{j,GABA}(t)}{dt} = -\frac{S_{j,GABA}(t)}{\tau_{GABA}} + \sum_k \delta_j(t - t_k) \tag{A5}$$

with τ_{GABA} = 10 ms; $S_{j,NMDA}$ obeys the second-order dynamics:

$$\frac{dS_{j,NMDA}(t)}{dt} = -\frac{S_{j,NMDA}(t)}{\tau_{NMDA}} + \alpha_{NMDA}x_j\left(1 - S_{j,NMDA}\right) \tag{A6}$$

$$\frac{dx_j(t)}{dt} = -\frac{x_j(t)}{\tau_x} + \sum_k \delta_j(t - t_k) \tag{A7}$$

where $x_j(t)$ is an intermediate gating variable, τ_{NMDA} = 100 ms, α_{NMDA} = 0.5 kHz, and τ_x = 2 ms.

Apart from several parameters, there are two major differences between AN-I and AN-II. First, the connectivity strengths between neurons are different. In AN-I, the strength of synaptic connectivity between two pyramidal cells depends on the difference between their preferred directions, $\Delta\theta = |\theta_i - \theta_j|$. The dependence is Gaussian-like, i.e.,

$$W_{ij}^{E\to E} = W^{E\to E}(\Delta\theta) = J_-^{E\to E} + \left(J_+^{E\to E} - J_-^{E\to E}\right)\exp\left(-\frac{\Delta\theta^2}{2\sigma_{E\to E}^2}\right) \tag{A8}$$

where the dimensionless parameters $J_-^{E\to E}$ and $J_+^{E\to E}$ separately represent the strength of cross- and iso-directional connections, and $\sigma_{E\to E}$ is the connectivity width. $J_+^{E\to E} = 1.82$, $\sigma_{E\to E} = 18°$, and the value of $J_-^{E\to E}$ is determined by the normalization condition, i.e.,

$$\frac{1}{360^\circ}\int_{0^\circ}^{360^\circ} W^{E\to E}(\Delta\theta)d(\Delta\theta) = 1 \tag{A9}$$

The strength of synaptic connectivity between interneurons or between a pyramidal cell and an interneuron is uniform, i.e., $W_{ij}^{E\to I} = 1.0$, $W_{ij}^{I\to E} = 1.0$, and $W_{ij}^{I\to I} = 1.0$. All the recurrent connectivity remains consistent in simulations.

In AN-II, the connectivity between principal cells is absent; the strength of synaptic connectivity between principal cells and interneurons depends on their angular difference $\Delta\theta = |\theta_i - \theta_j|$:

$$W_{ij}^{E\to I} = W^{E\to I}(\Delta\theta) = J_-^{E\to I} + \left(J_+^{E\to I} - J_-^{E\to I}\right)\exp\left(-\frac{\Delta\theta^2}{2\sigma_{E\to I}^2}\right) \tag{A10}$$

$$W_{ij}^{I\to E} = W^{I\to E}(\Delta\theta) = G_{I\to E}\exp\left(-\frac{(\Delta\theta - \mu_{I\to E})^2}{2\sigma_{I\to E}^2}\right) \tag{A11}$$

with $J_+^{E\to I} = 1.6$, $\sigma_{E\to I} = 30^\circ$, $\mu_{I\to E} = 90^\circ$, and $\sigma_{I\to E} = 30^\circ$. $J_-^{E\to E}$ and $G_{I\to E}$ are separately determined by the normalization condition:

$$\frac{1}{360^{\circ}}\int_{0^{\circ}}^{360^{\circ}} W(\Delta\theta)d(\Delta\theta) = 1 \tag{A12}$$

For simplicity, the connectivity between interneurons is assumed to be uniform, i.e., $W_{ij}^{I\to I} = 1$.

Second, the background synaptic input and noise currents are also different between AN-I and AN-II. For AN-I, they are modeled by Poisson spike trains from other brain areas. The background synaptic inputs are all excitatory and mediated by AMPARs. This external input to neuron i is given by

$$I_{i,ext}(t) = g_{ext}\left(V_{i,m}(t) - V_E\right)S_{i,ext} \tag{A13}$$

with $S_{i,ext}$ obeying

$$\frac{dS_{i,ext}(t)}{dt} = -\frac{S_{i,ext}(t)}{\tau_{AMPA}} + \sum_k \delta_i\left(t - t_{k,ext}\right) \tag{A14}$$

g_{ext} is the maximum conductance ($g_{ext\to E}$ = 4.19 nS and $g_{ext\to E}$ = 3.13 nS) and τ_{AMPA} = 2 ms. A cue-related current of I_{cue} = 120 pA was applied for 250 ms to neurons with preferred directions within a 45° range centered at180°.

For AN-II, the background and noise inputs read:

$$I_{i,ext}(t) = I_{Back} + I_{i,Noise}(t) \tag{A15}$$

The excitatory background inputs are constant, i.e., $I_{Back}^{E} = 650$pA and $I_{Back}^{I} = 325$pA. The noise current is independent of each other and described by the Ornstein–Uhlenbeck process:

$$\tau_{Noise}\frac{dI_{i,Noise}(t)}{dt} = -I_{i,Noise}(t) + \eta_{Noise}\sqrt{\tau_{Noise}}n_i(t) \tag{A16}$$

where $n_i(t)$ is Gaussian white noise with zero mean and unit standard deviation, η_{Noise} = 150 pA (standard deviation of the noise), and τ_{Noise} = 2 ms.

The ODEs were numerically integrated using a second-order Runge–Kutta method with a time step of 0.02 ms. For AN-II, the noise current was calculated using the Itô integral. The initial membrane potentials of all neurons were randomly valued between − 60 and − 50 mV, and all gating variables were set to zero.

References

1. Compte, A., Brunel, N., Goldman-Rakic, P.S., Wang, X.-J.: Synaptic mechanisms and network dynamics underlying spatial working memory in a cortical network model. Cereb. Cortex **10**, 910 (2000)
2. Liu, F., Wang, X.-J.: A common cortical circuit mechanism for perceptual categorical discrimination and veridical judgment. PLoS Comput. Biol. **4**, e1000253 (2008)
3. Burak, Y., Fiete, I.R.: Accurate path integration in continuous attractor network models of grid cells. PLoS Comput. Biol. **5**, e1000291 (2009)
4. Knierim, J.J., Zhang, K.: Attractor dynamics of spatially correlated neural activity in the limbic system. Annu. Rev. Neurosci. **35**, 267 (2012)
5. Khona, M., Fiete, I.R.: Attractor and integrator networks in the brain. Nat. Rev. Neurosci. **23**, 744 (2022)
6. Couey, J.J., Witoelar, A., Zhang, S.-J., Zheng, K., Ye, J., Dunn, B., Czajkowski, R., Moser, M.-B., Moser, E.I., Roudi, Y., Witter, M.P.: Recurrent inhibitory circuitry as a mechanism for grid formation. Nat. Neurosci. **16**, 318 (2013)
7. Funahashi, S., Bruce, C.J., Goldman-Rakic, P.S.: Mnemonic coding of visual space in the monkey's dorsolateral prefrontal cortex. J. Neurophysiol. **61**, 331 (1989)
8. Yoon, K., Buice, M.A., Barry, C., Hayman, R., Burgess, N., Fiete, I.R.: Specific evidence of low-dimensional continuous attractor dynamics in grid cells. Nat. Neurosci. **16**, 1077 (2013)
9. Trettel, S.G., Trimper, J.B., Hwaun, E., Fiete, I.R., Colgin, L.L.: Grid cell co-activity patterns during sleep reflect spatial overlap of grid fields during active behaviors. Nat. Neurosci. **22**, 609 (2019)
10. Gardner, R.J., Lu, L., Wernle, T., Moser, M.-B., Moser, E.I.: Correlation structure of grid cells is preserved during sleep. Nat. Neurosci. **22**, 598 (2019)
11. Chaudhuri, R., Gercek, B., Pandey, B., Peyrache, A., Fiete, I.: The intrinsic attractor manifold and population dynamics of a canonical cognitive circuit across waking and sleep. Nat. Neurosci. **22**, 1512 (2019)
12. Gardner, R.J., Hermansen, E., Pachitariu, M., Burak, Y., Baas, N.A., Dunn, B.A., Moser, M.-B., Moser, E.I.: Toroidal topology of population activity in grid cells. Nature **602**, 123 (2022)
13. Giocomo, L.M., Zilli, E.A., Fransén, E., Hasselmo, M.E.: Temporal frequency of subthreshold oscillations scales with entorhinal grid cell field spacing. Science **315**, 1719 (2007)
14. Pastoll, H., Solanka, L., van Rossum, M.C.W., Nolan, M.F.: Feedback inhibition enables theta-nested gamma oscillations and grid firing fields. Neuron **77**, 141 (2013)
15. Lundqvist, M., Rose, J., Herman, P., Brincat, S.L., Buschman, T.J., Miller, E.K.: Gamma and beta bursts underlie working memory. Neuron **90**, 152 (2016)
16. Harvey, C.D., Collman, F., Dombeck, D.A., Tank, D.W.: Intracellular dynamics of hippocampal place cells during virtual navigation. Nature **461**, 941 (2009)
17. Hafting, T., Fyhn, M., Bonnevie, T., Moser, M.-B., Moser, E.I.: Hippocampus-independent phase precession in entorhinal grid cells. Nature **453**, 1248 (2008)

18. Colgin, L.L.: Rhythms of the hippocampal network. Nat. Rev. Neurosci. **17**, 239 (2016)
19. Ouchi, A., Fujisawa, S.: Predictive grid coding in the medial entorhinal cortex. Science **385**, 776 (2024)
20. Navratilova, Z., Giocomo, L.M., Fellous, J.-M., Hasselmo, M.E., McNaughton, B.L.: Phase precession and variable spatial scaling in a periodic attractor map model of medial entorhinal grid cells with realistic after-spike dynamics. Hippocampus **22**, 772 (2012)
21. Lundqvist, M., Herman, P., Miller, E.K.: Working memory: delay activity, yes! persistent activity? maybe not. J. Neurosci. **38**, 7013 (2018)
22. Daume, J., Kamiński, J., Schjetnan, A.G.P., Salimpour, Y., Khan, U., Kyzar, M., Reed, C.M., Anderson, W.S., Valiante, T.A., Mamelak, A.N., Rutishauser, U.: Control of working memory by phase–amplitude coupling of human hippocampal neurons. Nature **629**, 393 (2024)
23. Hasselmo, M.E., Giocomo, L.M., Zilli, E.A.: Grid cell firing may arise from interference of theta frequency membrane potential oscillations in single neurons. Hippocampus **17**, 1252 (2007)
24. Burgess, N.: Grid cells and theta as oscillatory interference: theory and predictions. Hippocampus **18**, 1157 (2008)
25. Buzsáki, G.: Theta oscillations in the hippocampus. Neuron **33**, 325 (2002)
26. Gonzalez-Sulser, A., Parthier, D., Candela, A., McClure, C., Pastoll, H., Garden, D., Sürmeli, G., Nolan, M.F.: GABAergic projections from the medial septum selectively inhibit interneurons in the medial entorhinal cortex. J. Neurosci. **34**, 16739 (2014)
27. Pignatelli, M., Beyeler, A., Leinekugel, X.: Neural circuits underlying the generation of theta oscillations. J. Physiol. Paris **106**, 81 (2012)
28. Erchova, I., Kreck, G., Heinemann, U., Herz, A.V.M.: Dynamics of rat entorhinal cortex layer II and III cells: characteristics of membrane potential resonance at rest predict oscillation properties near threshold. J. Physiol. **560**, 89 (2004)
29. Goutagny, R., Jackson, J., Williams, S.: Self-generated theta oscillations in the hippocampus. Nat. Neurosci. **12**, 1491 (2009)
30. Tahvili, F., Destexhe, A.: A mean-field model of gamma-frequency oscillations in networks of excitatory and inhibitory neurons. J. Comput. Neurosci. **52**, 165 (2024)
31. Cakan, C., Obermayer, K.: Biophysically grounded mean-field models of neural populations under electrical stimulation. PLoS Comput. Biol. **16**, e1007822 (2020)
32. Keeley, S., Byrne, Á., Fenton, A., Rinzel, J.: Firing rate models for gamma oscillations. J. Neurophysiol. **121**, 2181 (2019)
33. Novák, B., Tyson, J.J.: Design principles of biochemical oscillators. Nat. Rev. Mol. Cell Biol. **9**, 981 (2008)
34. Ermentrout, G.B., Chow, C.C.: Modeling neural oscillations. Physiol. Behav. **77**, 629 (2002)
35. Wang, X.-J.: Synaptic basis of cortical persistent activity: the importance of NMDA receptors to working memory. J. Neurosci. **19**, 9587 (1999)
36. Gu, Z., Alexander, G.M., Dudek, S.M., Yakel, J.L.: Hippocampus and entorhinal cortex recruit cholinergic and NMDA receptors separately to generate hippocampal theta oscillations. Cell Rep. **21**, 3585 (2017)
37. Wong, K.-F., Wang, X.-J.: A recurrent network mechanism of time integration in perceptual decisions. J. Neurosci. **26**, 1314 (2006)
38. Wang, T., Sun, J., Yang, F., Li, J., Wang, W., Liu, F.: Background synaptic input modulates the visuospatial working memory. Phys. Rev. E **104**, 024416 (2021)
39. Wang, Z., Wang, T., Yang, F., Liu, F., Wang, W.: Intrinsic theta oscillation in the attractor network of grid cells. iScience **26**, 106351 (2023)
40. Xue, C., Liu, F.: Structured synaptic inhibition has a critical role in multiple-choice motion-discrimination tasks. J. Neurosci. **34**, 13444 (2014)
41. Abbott, L.F., Chance, F.S.: Drivers and modulators from push-pull and balanced synaptic input. Prog. Brain Res. **149**, 147 (2005)
42. Berggaard, N., Seifi, M., van der Want, J.J.L., Swinny, J.D.: Spatiotemporal distribution of GABA(A) receptor subunits within layer ii of mouse medial entorhinal cortex: implications for grid cell excitability. Front. Neuroanat. **12**, 46 (2018)
43. Solanka, L., van Rossum, M.C.W., Nolan, M.F.: Noise promotes independent control of gamma oscillations and grid firing within recurrent attractor networks. eLife **4**, e06444 (2015)
44. Tukker, J.J., Beed, P., Brecht, M., Kempter, R., Moser, E.I., Schmitzet, D.: Microcircuits for spatial coding in the medial entorhinal cortex. Physiol. Rev. **102**, 653 (2022)
45. Zhang, G., Yu, K., Wang, T., Chen, T.-T., Yuan, W.-D., Yang, F., Le, Z.-W., Guo, S.-Q., Xue, Y.-Y., Chen, S.-A., Yang, Z., Liu, F., Cropper, E.C., Weiss, K.R., Jing, J.: Synaptic mechanisms for motor variability in a feedforward network. Sci. Adv. **6**, eaba4856 (2020).
46. Brunel, N.: Dynamics and plasticity of stimulus-selective persistent activity in cortical network models. Cereb. Cortex **13**, 1151 (2003)
47. Seeholzer, A., Deger, M., Gerstner, W.: Stability of working memory in continuous attractor networks under the control of short-term plasticity. PLoS Comput. Biol. **15**, e1006928 (2019)
48. Wu, Y.K., Zenke, F.: Nonlinear transient amplification in recurrent neural networks with short-term plasticity. eLife **10**, e71263 (2021)
49. Deco, G., Cruzat, J., Cabral, J., Knudsen, G.M., Carhart-Harris, R.L., Whybrow, P.C., Logothetis, N.K., Kringelbach, M.L.: Whole-brain multimodal neuroimaging model using serotonin receptor maps explains non-linear functional effects of LSD. Curr. Biol. **28**, 3065 (2018)
50. Herzog, R., Mediano, P.A.M., Rosas, F.E., Luppi, A.I., Sanz-Perl, Y., Tagliazucchi, E., Kringelbach, M.L., Cofré, R., Deco, G.: Neural mass modeling for the masses: democratizing access to whole-brain biophysical modeling with FastDMF. Netw. Neurosci. **8**, 1590 (2024)
51. Lowet, E., Roberts, M.J., Peter, A., Gips, B., De Weerd, P.: A quantitative theory of gamma synchronization in macaque V1. eLife **6**, e26642 (2017)

52. Mi, Y., Liao, X., Huang, X., Zhang, L., Gu, W., Hu, G., Wu, S.: Long-period rhythmic synchronous firing in a scale-free network. Proc. Natl. Acad. Sci. U.S.A. **110**, 4931 (2013)
53. Huo, S., Zou, Y., Kaiser, M., Liu, Z.: Time-limited self-sustaining rhythms and state transitions in brain networks. Phys. Rev. Res. **4**, 023076 (2022)